Structural models of glassy As$_2$S$_3$: Intermediate-range order and photostructural changes

Gerd Pfeiffer, C. J. Brabec, S. R. Jefferys, and M. A. Paesler

Department of Physics, North Carolina State University, Raleigh, North Carolina 27695-8202

(Received 31 October 1988)

Results for the first models built and computer relaxed specifically to simulate the structure of glassy As$_2$S$_3$ are reported. Topological and bond statistic constraints are first satisfied by construction of a mechanical model. The energy relaxation potential consists of bond-stretching, bond-bending, and lone-pair interaction terms where the force constants for the lone-pair term are derived from a fit to experimental bulk-modulus data. Good agreements between the calculated and measured density and radial distribution function are taken as first necessary conditions that the models are realistic. Information about intermediate-range order correlations in the relaxed models is then obtained from a new technique that examines dihedral-angle relationships. The x-ray scattering intensity calculated for the models shows a dependence on elements of intermediate-range order. Examining contributions of different coordination shells to the peak structure in the region of the first sharp diffraction peak, we find that manipulation of certain shell contributions to the total scattering intensity reproduces the changes observed experimentally with reversible photostructural changes in the glass.

I. INTRODUCTION

The structure of chalcogenide glasses has been a controversial issue for many years due to the lack of reliable experimental data for the structure beyond the first coordination shell. In contrast, the structure of crystalline As$_2$S$_3$ (orpiment) is a well-understood example of a layered crystal. The structure is based on pyramidal AsS$_3$ molecular units[1] that are linked together to form helices, each consisting of alternating S and As atoms. Helices are connected via bridging S atoms to form a two-dimensional layer structure which is held together by strong, covalent, intramolecular bonding forces. The interaction between the layers, on the other hand, is based primarily on weak, van der Waals, intermolecular forces. By association with the structure of orpiment, amorphous arsenic trisulfide, a-As$_2$S$_3$, has been widely believed to have a similar layered structure. The existence of outrigger rafts[2] and molecular clusters[3] has been put forward as structural models for the glass. It is known from vibrational spectroscopy that short-range order (SRO) in the glass is determined by the same AsS$_3$ pyramids found in the crystal.[4] But due to the lack of symmetry required for spectroscopy, information about larger structural units is not readily available. It is, however, the structure beyond the first coordination shell, the realm of intermediate-range order (IRO), where the key to understanding many fundamental properties of these materials lies. As a first step, recent extended x-ray-absorption fine-structure (EXAFS) studies[5] provide increased understanding of structural relationships involving configurations larger than simple four atom pyramids.

II. CONTINUOUS RANDOM NETWORK MODEL

A. Introduction

Structural models have been recognized as valuable tools for gaining an understanding of the structure of noncrystalline solids.[6] For solids with primarily covalent bonding, the appropriate type of model is a continuous random network (CRN). There are two basic methods to generate a CRN model. The first is to actually build a physical stick-and-ball model and the second is to generate a structure in the computer by an appropriate algorithm. The use of stick-and-ball models has the disadvantage that stress built into the model, especially sagging of the structure due to gravity, displaces the atoms from their equilibrium positions. Furthermore, the size of the model is limited for practical reasons to a few thousand atoms or, equivalently, several tens of angstroms in diameter, which is very small on a macroscopic scale. Hence, finite-size effects can become very troubling in the calculation of physical quantities [i.e., x-ray- or neutron-scattering intensity, $I(k)$, and the radial distribution function, RDF]. On the other hand, purely computer-generated models often cannot achieve perfect connectivity,[7] yielding voided, dendritic, or globular structures that do not fill space uniformly.

The quality of model RDF's can be greatly improved by means of energy relaxation, i.e., "moving" every atom to a position of lower potential energy using a computer, indicating that the resulting structures are more realistic. For elemental materials (e.g., Si, Ge, and As), reasonable results have been obtained from relaxed stick-and-ball models[8-10] and the sillium model.[11] At the same time, compound materials have proved to be much more difficult to model than elemental amorphous solids. We are aware of only a few attempts to model the structure of g-As$_2$S(Se)$_3$. In one case, a Monte Carlo method was used to fit the model RDF to experimental data on As$_2$Se$_3$.[12] The setback of this work is that considerations to ensure that the atoms are located in energetically stable positions are not included. Another model[13] is flawed with the presence of a high number of fourfold rings. There has been no spectroscopic evidence supporting the existence of such small rings and the bond distor-

tion necessary to create such a structure would be considerable. The RDF's of some of the models generated by Fowler and Elliott[14] show good agreement with experimental data and also reproduce the first sharp diffraction peak in the $I(k)$ spectrum, but appear to be unrealistic due to high deformation energies. Furthermore, no information on the models' IRO is mentioned.

The strategy pursued with our work was to build stick-and-ball models of several hundred atoms with correct bond angles and then to computer-relax the structure. We feel that a combination of stick-and-ball models as the starting point and an iterative energy-relaxation procedure minimizes the principal setbacks of the two individual approaches. The careful choice of the model parameters (i.e., correct coordination numbers, bond angles, and relaxation parameters) is the key to developing realistic models. Together with EXAFS data,[5] our approach is designed to address the issue of IRO in chalcogenide glasses.

B. The stick-and-ball models

Stoichiometric As_2S_3 is known from a great deal of experimental data to exhibit a strong tendency towards chemical ordering. That is, heteropolar As—S bonds are energetically favored over homopolar As—As and S—S bonds. Hence, the glass is a prototype compound for a homogeneous chemically ordered CRN model incorporating mostly heteropolar bonds between twofold-coordinated S atoms and threefold-coordinated As atoms.

Two stick-and-ball models (of 445 and 700 atoms, referred to as models A and B, respectively) were built independent of each other and have yielded similar RDF's but subtly different IRO. Model B was built by a student who had no preconceived notion about the structure of As_2S_3, whereas model A was built by a scientist familiar with discussions about the structure of amorphous and crystalline materials. The models consisted of plastic balls representing the twofold-coordinated S atoms and the threefold-coordinated As atoms with bond angles of 99° for both types of atoms. The connection between the balls was flexible enough to allow for a 10% spread in bond angle and bond length. No homopolar (wrong) bonds and no internal dangling bonds were allowed and all surface (i.e., undercoordinated) atoms were chosen to be S atoms.

C. Relaxation

The computer relaxation serves two distinct purposes in our work: (1) to relax strain built into the model, and (2) to determine the influence of subtle features of the interatomic potential which cannot be built into the stick-and-ball models but play a very important role in atomic arrangements in the material. The potential consists therefore of two different contributions: a conventional part accounting for the covalent-bonding forces and a novel part simulating the interaction between the lone-pair (LP) electrons on chalcogen atoms. To model the covalent-bonding forces, the valence-force-field (VFF) formulation[15] was used. In this approach, deviations from atomic equilibrium positions, Δr and $\Delta\theta$, are related to the potential energy[15] by

$$V = \tfrac{1}{2} \sum k_r (\Delta r)^2 + \tfrac{1}{2} \sum k_\theta (r_0 \Delta\theta)^2$$
$$+ \tfrac{1}{2} \sum k_{rr'} (\Delta r \, \Delta r')^2 \ . \tag{1}$$

Principally, the VFF approach includes a number of additional terms describing the interactions between the central atom and its nearest neighbors. These terms were omitted because their force constants are very small[16] compared to k_r and k_θ. Furthermore, the VFF expansion (1) was truncated after the first two terms in our calculation. Neglecting the $k_{rr'}$ term simplifies the computation considerably and still allows for observation of the systematic effect of the relaxation. Whereas only one stretching force constant k_r is needed, two bending force constants, $k_\theta^{(As-S-As)}$ and $k_\theta^{(S-As-S)}$, are required, reflecting bending motions centered on S and As atoms, respectively. Nonbonded LP charge clouds on chalcogen atoms have been recognized as an important factor in the atomic and electronic structure of chalcogenide materials,[17-19] so that a relaxation potential based solely on covalent-bonding forces would be incomplete.

In selenium, a chalcogen with a valence-electron shell configuration similar to sulfur, energetically favored arrangements in which the LP charge clouds on two adjacent atoms are aligned roughly perpendicular to each other lead to helical, chainlike structures.[19] In the compound As_2S_3 the situation is somewhat different because the chalcogen atoms are bonded to As atoms instead of other chalcogens. Nevertheless, the underlying effect is similar on a qualitative basis because, in Se, the repulsion between the LP orbitals on second-nearest neighbors seems to be responsible for the ordering of the dihedral angles.[20] Similar helical configurations may exist in g-As_2S_3, with the LP interaction between second-nearest-neighbor S atoms as the driving force for this structural ordering.

In the $3s^2 3p^4$ valence-shell electron configuration of sulfur, two of the $3p$ orbitals participate in covalent bonds with neighboring As atoms, whereas the two other $3p$ orbitals remain as nonbonded p-π or LP electrons giving rise to interesting structural effects. The simulation of the quantum-mechanical interaction between the LP orbitals on different chalcogen atoms is therefore an important step in developing a more realistic relaxation algorithm for structural models of chalcogenide glasses. A quantitative description of this interaction which is computationally tractable for the relaxation algorithm is not easily at hand. However, a simple phenomenological description of the basic physics can be applied. To better visualize the situation, we introduce a vector ω_i pointing from the nucleus to the center of one LP orbital for each S atom. If the two sulfur atoms under consideration are sufficiently far apart, the interaction between LP orbitals tends to align the two vectors ω_i and ω_j in a "cross" configuration, i.e., they are located in two parallel planes and the projections of ω_i and ω_j on a common plane form an angle of 90°. The alignment can be thought of as the result of two forces, one responsible for the 90° cross

configuration [Fig. 1(a)] and the other to establish an angle of 90° between ω_i and the vector r_{ij} connecting the two S atoms under consideration [Fig. 1(b)]. These two forces can be expressed in terms of the angles ϕ_j and ψ_j, respectively, and their deviations from the 90° configuration. The forces are harmonic in the simplest approach, with an additional exponential term $(e^{-\gamma r}/r)$ to establish a reasonable range for the interaction. The calculation is carried out for each S atom and all of its neighboring S atoms within a sphere of radius 6 Å since the influence of sulfur atoms further than 6 Å from the central S atom is negligible.

Combining the VFF approach with the considerations for the lone-pair interaction, the total relaxation potential was the sum of two basic components:

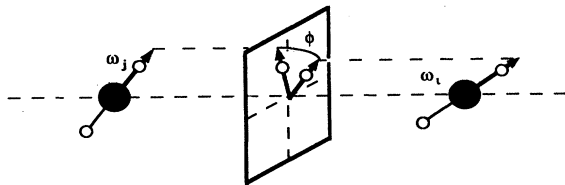$$\Phi_{\text{total}} = \Phi_{\text{VFF}} + \Phi_{\text{lone pair}} , \qquad (2)$$

with

$$\Phi_{\text{VFF}} = \frac{1}{2} \sum k_r(\Delta r)^2 + \frac{1}{2} \sum k_\theta(r_0 \Delta \theta)^2 \qquad (3)$$

and

$$\Phi_{\text{lone pair}} = \frac{1}{2} \sum_j k_{\text{pt}}(\psi_j - \psi_0)^2 \left[\frac{e^{-\gamma r_{ij}}}{r_{ij}} \right] + \frac{1}{2} \sum_j k_{\text{cr}}(\phi_j - \phi_0)^2 \left[\frac{e^{-\gamma r_{ij}}}{r_{ij}} \right] . \qquad (4)$$

The force constants k_r and k_θ are calculated from vibrational experiments,[15] whereas k_{pt} and k_{cr} (for point and cross, respectively) are found by fitting the bulk
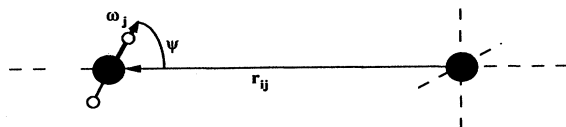
(a)

(b)

FIG. 1. Definition of the angles ϕ and ψ used in Eq. (4) for the lone-pair potential. (a) The angle between the projections of ω_j and ω_i on a plane perpendicular to a line joining atoms i and j is measured by ϕ. (b) The angle ψ describes the relationship between the vector r_{ij} which connects the two sulfur atoms i and j and ω_j.

modulus K_T calculated from a cluster of atoms in the center of the model to experimental data[21] using

$$K_T = V \frac{\partial^2 \Phi}{\partial V^2} . \qquad (5)$$

In this calculation, only the lone-pair term (4) of the total potential is used since the weak noncovalent-bonding forces exhibit a much stronger dependence on compression than the covalent bonds.[21] The volume decrease to simulate compression of the model was accomplished by scaling all covalent-bond lengths, then relaxing the structure at constant volume, leaving the force constants unchanged. Since this approach does not distinguish between the components of the lone-pair potential associated with k_{cr} and k_{pt}, the two force constants are treated on an equal footing.

The choice for the relaxation parameters (see the Appendix), and especially k_{cr} and k_{pt}, was verified by comparing the nearest-neighbor distances from the pair distribution functions of the fully relaxed models with experimental data. Deviations from these values give incorrect nearest-neighbor distances. The effect of larger values for k_{cr} and k_{pt} is mainly a broadening and shift to lower radii of the first peak in the S-S pair distribution function, signifying unphysically small S-S distances. If the two constants are taken to be too small, the S-S peak remains very broad compared to the experimental data.

The computer algorithm relaxes one atom at a time, proceeding outward from the center of the model to dissipate stress. For an atom to be relaxed, the potential is calculated for points on a three-dimensional grid and the atom is then moved to the location of lowest potential energy. The algorithm needed about 2500 iterations until the average change in the atomic positions and the total potential, defined as the sum of the potential energy of the individual atoms, became very small and, thus, the model was considered to be fully relaxed. An increased number of iterations leads only to insignificant changes in atomic positions, total potential, and angular stress.

D. Radial distribution function

In the absence of crystalline long-range order, the RDF is a useful tool for representing real-space structural information about amorphous solids. The RDF, $J(r)$, defined as the average number of atoms per unit spatial interval at distance r from an atom at the origin, consists of a series of well defined peaks at small r:

$$J(r) = 4\pi r^2 \rho(r) . \qquad (6)$$

Each peak represents a definite atomic correlation in the material. Due to the lack of long-range order, these correlations become less significant for large distances, causing the discrete peaks to overlap and broaden into an average density parabola proportional to $4\pi r^2$ at large r. As an alternative method of representation, the correlation function

$$D(r) = \left[\frac{J(r)}{r} - 4\pi r \rho^0 \right]$$

$$= \frac{2}{\pi} \int_0^\infty F(k)\sin(kr)dk \tag{7}$$

can be used. $D(r)$ can be calculated directly from modeling data and is also obtained as the Fourier transform of the reduced experimental x-ray- or neutron-scattering intensity. This allows for a direct check of modeling against experimental data. However, a RDF does not uniquely characterize a structure and indeed, different model structures that are based on the same SRO parameters can have very similar RDF's.

As all interatomic distances are readily available from the recorded atomic positions in the model, computation of a RDF amounts ideally to a simple frequency count of these correlations calculated from every atom. Nevertheless, the task of calculating the RDF from model data becomes quite formidable when the consequences of the models' finite size are taken into account. As one possible method of reducing finite-size effects, all atoms with a radius from the center of the model greater than r_0, with r_0 as the radius of the centermost surface atom, are excluded from the calculation. Applying this criterion to the two models, about 75% of the total number of atoms (445 and 700) were to be left out, thereby resulting in poor statistics. As a compromise, the maximum radius from the center, r_m, for an atom to be included in the calculation was chosen to be $r_m = 0.75r_a$, where r_a is the average radius of the model. To minimize the influence of atoms far from the center of the model, the contribution from each atom was multiplied by a weighting factor[22]

$$\frac{1}{W} = 1 - \frac{3}{4}\frac{r_i}{r_a} + \frac{1}{16}\left[\frac{r_i}{r_a}\right]^3, \tag{8}$$

with r_i the distance from the center to the atom. The calculated RDF follows the average density parabola until the maximum radius of the model is reached and then begins to fall off. The deviation begins at approximately $0.75r_a$ and the information contained in the RDF beyond this point is considered meaningless and is not included in any interpretation.

For a model to be physically reasonable, the calculated and the experimentally measured density for the material have to match closely. The density $\rho(r)$ as a function of radius from the geometric center of the model is shown in Fig. 2, together with the experimental value indicated by a dotted line. Averaging the density over a range from 6 to 13 Å, a density deficit of 5.7% is obtained for model A and 11.7% for model B. The higher density of model A seems to indicate that this model is more realistic than model B. The density function for both models begins to fall off for radii of 13 Å or more, reflecting the finite size of the structures.

Using the technique outlined earlier, the RDF, $J(r)$, was calculated for both models, and the results are presented in Fig. 3, together with experimental data.[23] To allow for a more unbiased examination, the model data are shown without thermal broadening in order to
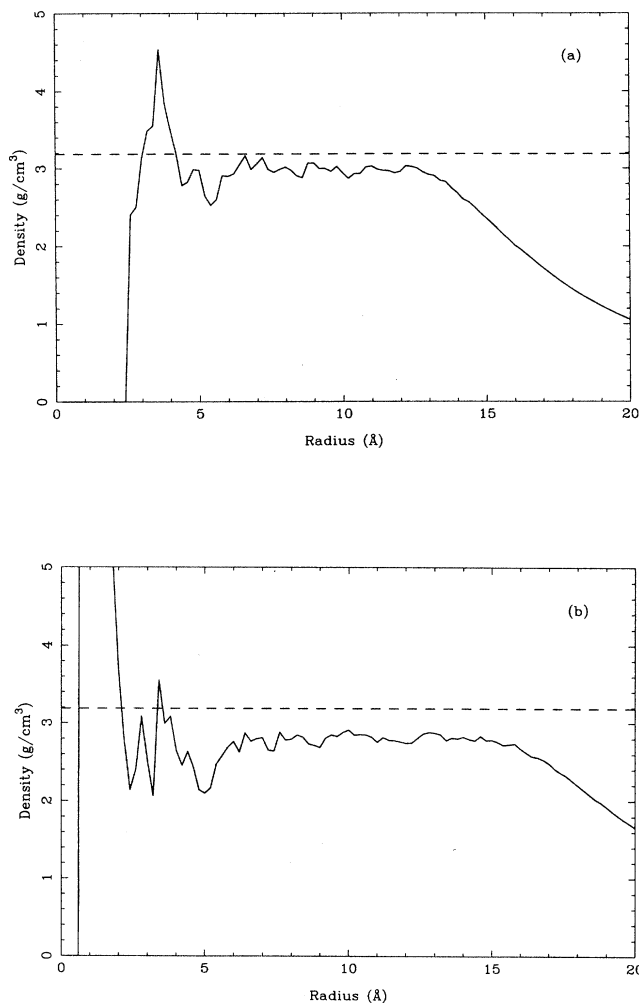

FIG. 2. Density as a function of radius. (a) Computed from relaxed model A and (b) from relaxed model B. Since the calculation was carried out from the center of the model, only information for radii greater than 5 Å is meaningful. Averaging the density between 6 and 13 Å, model A comes within 5.7% of the experimental value for g-As_2S_3, whereas model B shows a density deficit of 11.7%. The finite size of the models causes the density to fall off for large distances.

avoid the somewhat arbitrary procedure used to incorporate thermal broadening into the peak structure. Both models result in very similar distribution functions and match the experimental curve closely in a systematic manner, thus emphasizing that the structures are indeed noncrystalline and have not relaxed into a state possessing long-range order. Position and amplitude of the first two peaks for the model data reflect the SRO parameters built into the model and the relaxation process. The absence of longer-range atomic correlations due to the limited model size causes the model RDF's to deviate from the r^2 parabola for the experimental data for larger radii. Although our models are an idealization of the material, the good agreement between relaxed and experimental data is a clear suggestion that they are realistic. Hence,
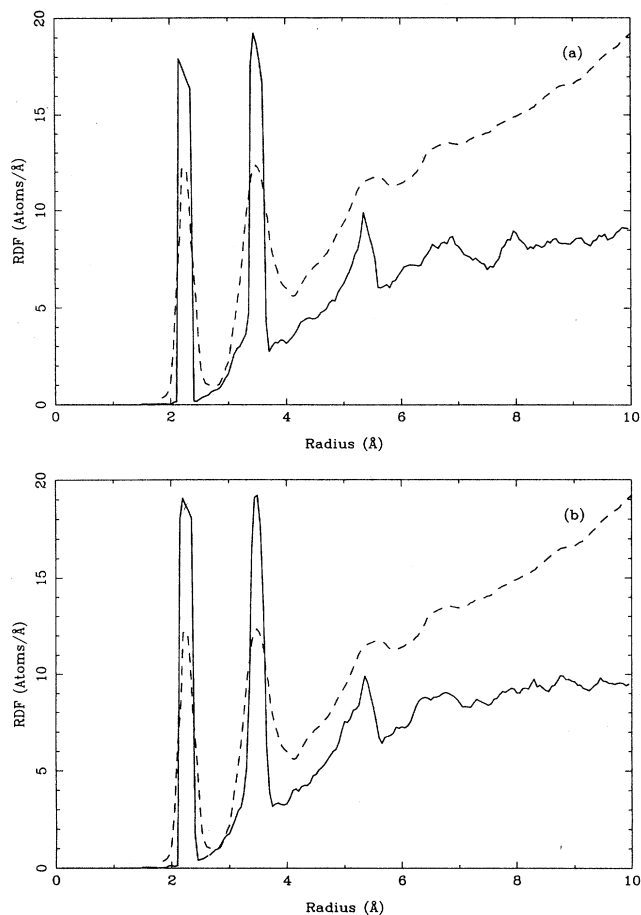
FIG. 3. Plot of the radial distribution function $J(r)$ vs radius. (a) Calculated from relaxed model A and (b) calculated from relaxed model B. Solid line: RDF computed from the relaxed model without thermal broadening. Dotted line: experimental RDF (see Ref. 23).

they pass a necessary zeroth-order criterion for being physically reasonable and can be used to ask questions about IRO.

III. INTERMEDIATE-RANGE ORDER

A. Dihedral angle relationships

The concept of dihedral angles can be used to characterize correlations between structural units beyond the first coordination shell for both the crystalline and the amorphous state. According to the definition of dihedral angles (Fig. 4), each S atom has two dihedral angles (θ_1 and θ_2) associated with it, each of which describes the orientation of one neighboring AsS_3 pyramidal unit with respect to the central S atom. Due to symmetry, only two distinguishable sulfur environments occur within a layer of c-As_2S_3: S atoms within a helical —As—S—As—S—As— chain, and S atoms bridging between two different helices, referred to as h-S and b-S sites, respectively. These two S-atom environments are reflected in different values for the pair of dihedral angles on each S,
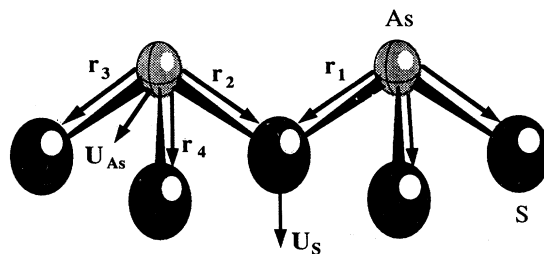
$$r_S = r_1 + r_2 \qquad\qquad r_{As} = r_2 + r_3 + r_4$$

$$U_S = \frac{r_S}{|\,r_S\,|} \qquad\qquad U_{As} = -\frac{r_{As}}{|\,r_{As}\,|}$$

Dihedral Angle : $\Theta = \cos^{-1}\ (U_{As} \bullet U_S)$

FIG. 4. Definition of the dihedral angle as used in this work. A pair of dihedral angles, θ_1 and θ_2, on a sulfur atom describes the orientation of two neighboring AsS_3 pyramidal units with respect to each other.

where b-S sites have two identical (163°, 163°) and h-S sites have two different (68°, 146°) dihedral angles. To better visualize the two distinct S sites, we plot one dihedral angle as the ordinate and the other dihedral angle as the abscissa for the two S sites in c-As_2S_3 on a two-dimensional plot (Fig. 5). For convenience, the greater of
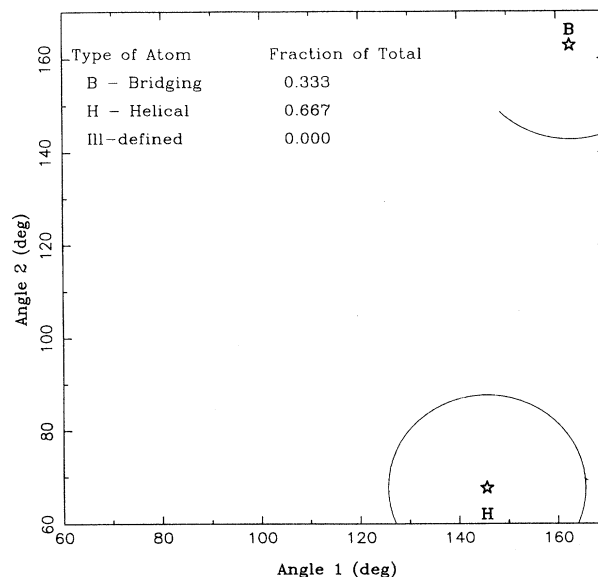

FIG. 5. Scatter plot of S-atom environments represented by the two dihedral angles, θ_1 and θ_2, which define the S-atom environment. The ordinate represents one dihedral angle, whereas the abscissa represents the other. The greater of the two dihedral angles per sulfur atom is plotted as the ordinate. The two different S-atom bonding sites occurring in c-As_2S_3, the bridging- (b-S) and helical- (h-S) sulfur sites, are shown.

PFEIFFER, BRABEC, JEFFERYS, AND PAESLER

these dihedral angles is taken arbitrarily as the ordinate.

Figure 6 shows the dihedral angle relationships for models A and B plotted in the same fashion as in Fig. 5. In the computation of dihedral angle relationships, all surface atoms have to be excluded since they are less constrained and their positions are therefore very flexible compared to internal fully coordinated atoms. A truly random distribution of dihedral angle relationships in the model would result in uniform coverage on such a plot.

Clearly, the coverage of the plot with points representing the environments of S atoms is not uniform. Although there is some spread in the values, significant clustering occurs about the values for crystalline h-S and b-S sites. This means that topological constraints built into the CRN model (twofold coordination for S atoms, threefold coordination for As atoms, and the appropriate bond angles) favor dihedral angle configurations similar to the crystal. These topological constraints induce a definite degree of structural ordering beyond the first coordination shell in the range of IRO.

Next, we examine the influence of the energy relaxation on dihedral angle relationships. Comparing the plots for the fully relaxed models shown in Fig. 7 with the unrelaxed data (Fig. 6), we notice that the relaxation process has a considerable influence on the S sites in both models. Qualitatively, increased clustering about the crystalline-S-site locations, especially the h-S site, can be observed, indicating that the relaxed model structures exhibit ordering in terms of crystalline S sites. In earlier work[24] on model A using a relaxation potential without the lone-pair term, it was shown that helical ordering also does occur, but it is much weaker without the LP term. The degree of helical ordering can be quantified by considering the number of points, i.e., dihedral angle relationships, in Fig. 6 relative to the h-S and b-S sites. For orpiment, the ratio of S atoms in bridging to S atoms in helical configurations is 1:2. To get a qualitative feeling for the effect, all dihedral angle configurations within a circle of radius 20° from the b-S site in Fig. 6 are taken to be similar enough to the bridging configuration in c-As_2S_3 to be classified as b-S. An equivalent criterion can be applied to dihedral angle configurations in the proximity of the crystalline h-S site. The results are tabulated for the two relaxed models in Table I. Most notably, more than 60% of the S configurations are ill defined in terms of the crystalline sites, underscoring the fact that the models are truly noncrystalline. Remarkably, model A exhibits clearly more helical character, whereas the ratio of b-S to h-S is very close to the crystalline value of 0.5 for model B. The low ratio of b-S to h-S for model A demonstrates that there is not a sufficient amount of b-S sites present to permit coherent linking of helices into planar structures, hence underscoring the argument that helices are important structural elements in the glass and planes are not. Further analysis indicates that model A, as will be discussed in Sec. II B, produces a more realistic x-ray-scattering spectrum, thereby suggesting that its helical
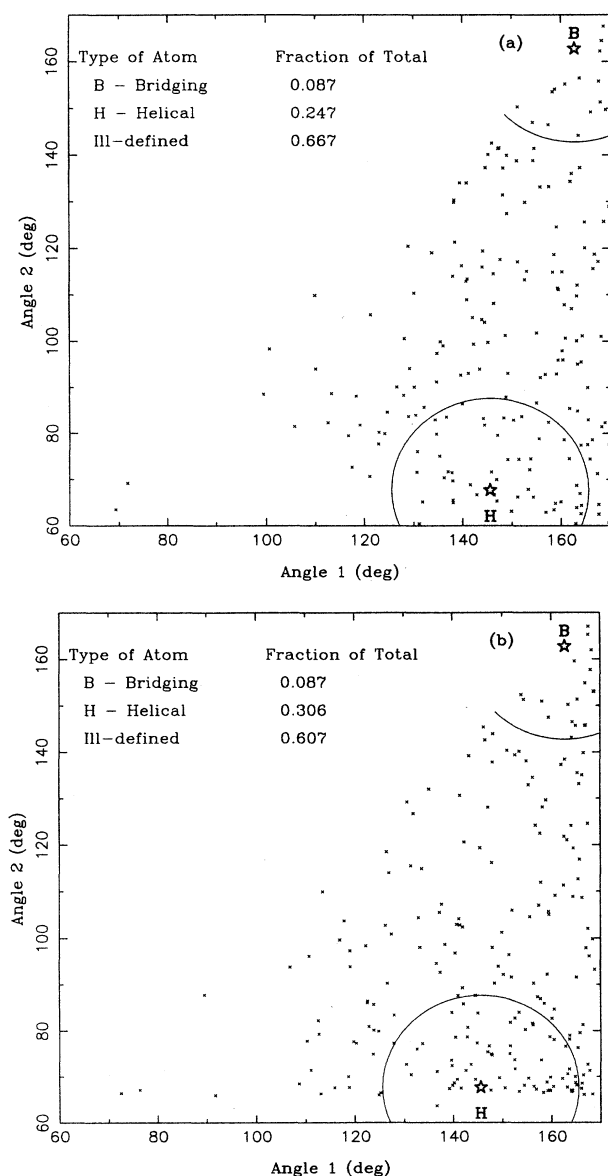

FIG. 6. Scatter plot of S-atom environments in the unrelaxed model. (a) Calculated from model A and (b) from model B. Each data point represents one S atom in the model. Clustering about the values of crystalline helical- and bridging-sulfur atom sites can be observed. Points within the circles of radius 20° about the b-S and h-S points are taken to be b-S- and h-S-like, respectively. The fractions of b-S, h-S, and ill-defined sulfur (i-S) atoms are shown in the upper left-hand corner.

TABLE I. Fraction of bridging, helical, and ill-defined S atoms for relaxed model A, model B, and c-As_2S_3. Also given is the ratio of bridging S to helical S for each case.

Model	b-S	h-S	i-S	$\left[\dfrac{[b\text{-}S]}{[h\text{-}S]}\right]$
A	0.087	0.306	0.607	0.28
B	0.124	0.245	0.632	0.51
c-As_2S_3	0.333	0.667	0	0.5

character is a more realistic picture for the real glass. Generally, the number of helical configurations increases upon relaxation at the expense of ill-defined S sites, whereas the bridging sites remain essentially unchanged. For the more realistic structure of model A, we conclude that relaxation clearly promotes ordering of the model in terms of helices, but does not increase coherent linking of helices into layer structures of IRO. A possible explanation for this behavior can be developed in analogy to a-Se, for which it has been shown[19] that the driving force
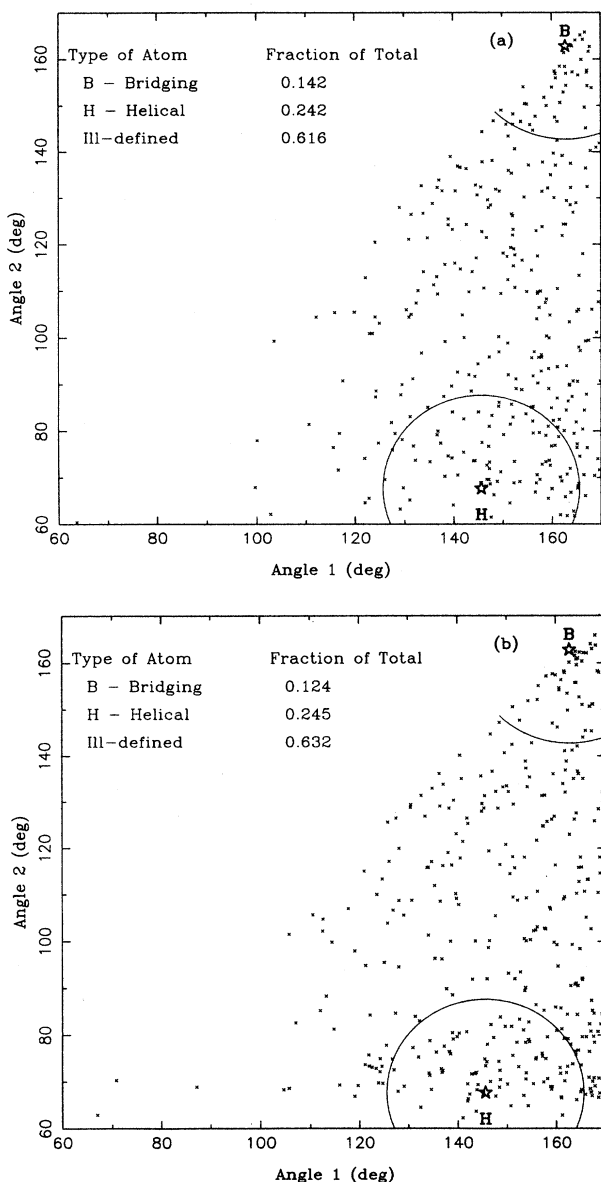

FIG. 7. Scatter plot of S-atom environments in the relaxed model. (a) Calculated from model A and (b) from model B. Points within the circles of radius 20° about the b-S and h-S points are taken to be b-S- and h-S-like, respectively. Increased clustering about the crystalline S-atom bonding sites occurs with relaxation. Nonuniform coverage of the plot indicates presence of intermediate-range order.
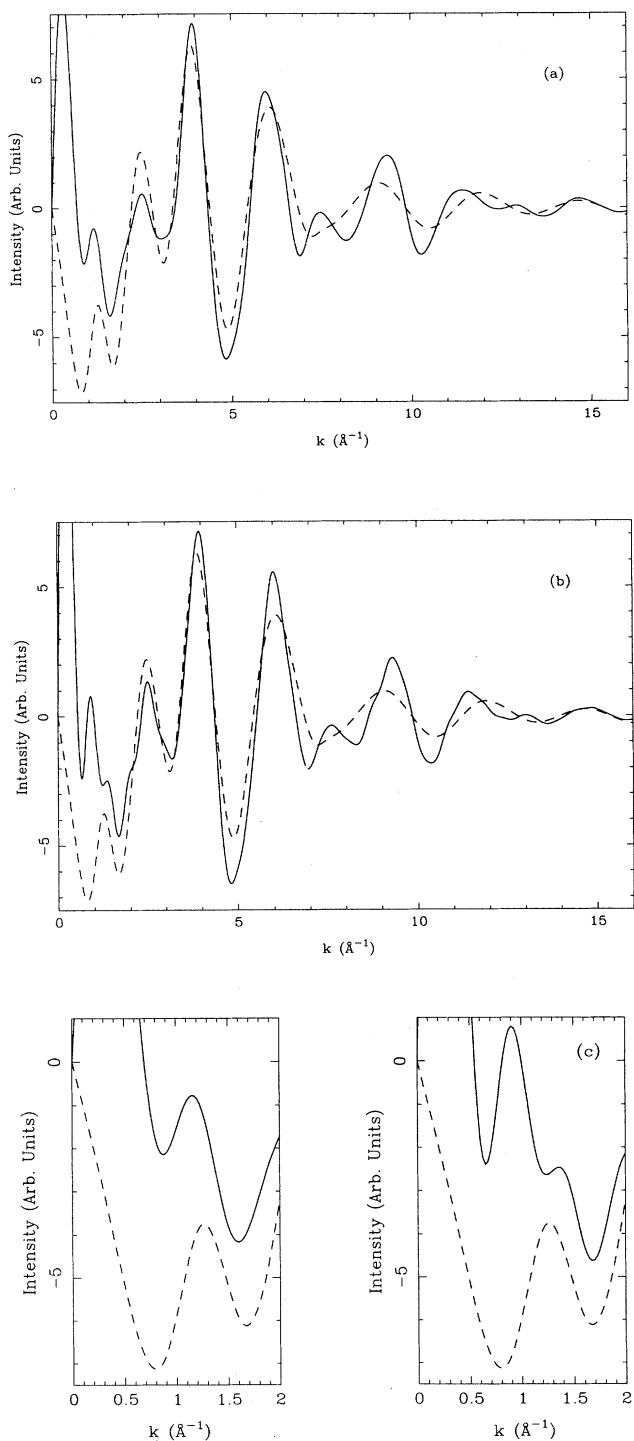
for ordering of dihedral angles is the orientation of LP orbitals on neighboring atoms.

The striking differences in IRO between models A and B may seem surprising at first sight, but appear more logical in the light of their history. Since Model A was built by a scientist interested in the structure of g-As$_2$S$_3$, a subjective bias to incorporate known structural elements, i.e., helices, can be assumed, thereby explaining the higher degree of helicity in this case.

B. X-ray-scattering intensity

X-ray- and neutron-diffraction techniques play an important role in the determination of short- and intermediate-range order in noncrystalline solids. The absence of long-range order gives diffraction spectra consisting of broad, spread out, features. For the model structures, the scattering intensity can be calculated using the Debye equation

$$I(k) = \sum_{m=1}^{n_t} \sum_{n=1}^{n_t} f_m(k) f_n(k) \frac{\sin(k r_{mn})}{k r_{mn}} , \qquad (9)$$

where the summations extend over all atoms in the model (n_t) with $f(k)$ as the atomic form factor of the appropriate type of atom, and r_{mn} as the distance between atoms m and n. A direct link between scattering and real-space structural data is established by the relationship between the reduced scattering intensity[25] $F(k)$ and the total correlation function $D(r)$,

$$F(k) = k \left[\frac{I(k)/N - \langle f^2(k) \rangle}{\langle f(k) \rangle^2} \right]$$

$$= \int_0^\infty 4\pi r [\rho(r) - \rho^0] \sin(kr) dr , \qquad (10)$$

with $\langle f(k) \rangle$ as the weighted average of the form factors of the two atomic species. To better facilitate the numerical calculation for $F(k)$, the integral in Eq. (10) can be replaced by a sum over all discrete radii. Since the pair correlation functions are available only over a limited radial range, a damping factor $M(r) = \exp(-\alpha r^2)$ has to be included. The reduced scattering intensity for the model can therefore be written as

$$F(k) = \frac{\sum_{r > 0}^{r_{max}} x_i f_i(k) f_j(k) d_{ij}(r) M(r) \sin(kr)}{\langle f(k) \rangle^2} , \qquad (11)$$

with an implied summation over the four pair correlation functions for the binary alloy and x_i as the fractional composition.

Figure 8 shows a comparison of the reduced scattering intensity calculated for models A and B with experimental data.[23] The overall agreement between calculated and experimental data is reasonable for both models. However, both models show deviations for very small values of k ($k < 0.5$ Å^{-1}) and in the region $k \approx 7.5$ Å^{-1}. The discrepancy for very small k is attributed to the finite size of the model, which does not give any information about

FIG. 8. Reduced x-ray-scattering intensity, $F(K)$, vs wave vector k for the two models. Solid line: (a) spectrum calculated from model A, and (b) calculated from model B using Eq. (11). Dotted line: experimental x-ray-scattering spectrum (see Ref. 23). (c) Low-k region on an expanded scale for the two previous plots. Model A (left) and model B (right). The curve from model A gives a much better match for position and amplitude of the first sharp diffraction peak at $k_F \approx 1.16$ Å^{-1}.

atomic correlations beyond 12 Å, corresponding to a value for the scattering vector $k_{min} = 2\pi/r_{max} = 0.52$ Å^{-1}. At about 7.5 Å^{-1}, both calculated curves show a peak instead of a slight shoulder in the experimental data. A similar deviation is suggested in the $I(k)$ spectra calculated by Fowler et al. from their models.[14] At the present time, the interpretation of this peak is not clear.

Next, we would like to turn our attention to the first sharp diffraction peak which occurs for g-As$_2$S$_3$ at a value of $k_F \approx 1.16$ Å^{-1}. The origin of this peak has been the matter of widespread controversy since it is located close to the orpiment (020) reflection, which arises from interlayer correlations.[1,26] Thus, many attempts have been made to identify the origin of the first sharp diffraction peak as being related to the separation of layers believed to be also present in the glass.[26−29] This interpretation seems questionable since the first sharp diffraction peak occurs not only in g-As$_2$S$_3$, but also in nonlayered materials like a-SiO$_2$ and a-GeSe$_2$. In fact, the same peak structure at low k can be derived from a model of randomly packed and partially polymerized As$_4$S$_4$ molecules.[23,30] Furthermore, even models based on unrealistic structures as indicated by high deformation energies[14] match the experimental $I(k)$ spectrum including the position of the first sharp diffraction peak reasonably well. Thus great care has to be taken to ensure that the model is realistic when relating its structure to features in the x-ray-scattering spectrum.

A comparison of the spectra calculated from models A and B [Fig. 8(c)] reveals remarkable differences in the region between 0.5 and 2.0 Å^{-1} where the first sharp diffraction peak occurs. Model B displays two maxima, one shifted to higher k and the other shifted to smaller k values from the experimental first sharp diffraction peak, and a minimum at the position of the experimental first peak. Model A, on the other hand, reproduces the maximum in the correct location and lacks entirely the minimum of model B, thus giving good systematic agreement with the experimental data in the low-k region and thereby suggesting that the structural features of this model are more realistic. By visual inspection of the structures and referring to the discussion in Sec. III A, it is apparent that both models used in this work are more polymeric than planar. The fact that model A successfully reproduces the position and shape of the first sharp diffraction peak without relying on a layered or planar structure emphasizes the important role of helices in the structure of g-As$_2$S$_3$. The presence of helical elements seems to be of critical importance for the first sharp peak, but it is uncertain whether a specific real-space correlation that might affect the sin(kr) term in Eq. (11) in this region in k space can be identified. However, the evidence presented here and the temperature and composition dependence[29] of the peak strongly support the notion that a correlation between the structure and the first sharp peak does exist. The range of real space correlations that could influence the first sharp peak points to the regime of IRO, but it appears premature to postulate a unique association between the peak and specific structural configurations characteristic for the glassy state.

C. Reversible photostructural changes

Chalcogenide glasses exhibit a light-induced red shift of the optical absorption edge which is reversible upon thermal annealing just below the glass-transition temperature.[31] Experimental evidence clearly suggests that the presence of chalcogen atoms is crucial for *reversible* photostructural changes, or photodarkening, to occur and the magnitude depends on the specific type of the chalcogen atom.[32] Photodarkening, which does not occur in crystalline materials, is a structural rearrangement unique to the glassy phase. However, the mechanism for this structural rearrangement is still under investigation. The EXAFS data[5] have been interpreted as a light-induced rotation of two AsS$_3$ pyramidal units joined at a particular S site with respect to each other about their respective bond with the central S atom. This rotation is equivalent to a distortion of dihedral angle relationships which define helices and an increase in structural randomness.[5]

In the x-ray-scattering spectrum, a broadening and shift to higher k values is found for the first sharp diffraction peak with photodarkening[33] (Fig. 9). At the same time, the difference in amplitude between the maximum at k_F and the adjacent minimum at higher k decreases, amounting to an increase in structural randomness in the material. In association with the interpretation of the first sharp diffraction peak as the correlation between layers in the glass, the shift has been interpreted as a decrease in interlayer separation with photodarkening. This interpretation is difficult to reconcile with the experimentally observed volume expansion associated with photodarkening. Together with the ambiguity of the layer interpretation as discussed in Sec. III B, we feel that layers are not appropriate structural units for discussing the microscopic mechanism of photodarkening.

In an attempt to pinpoint the range of real-space correlations involved in the changes in the first sharp diffraction peak with photodarkening, the model $I(k)$ spectrum is fitted to an experimental spectrum of the material in the photodarkened state. Trying to simulate the shift with photodarkening, contributions within a certain range were excluded from the sum in Eq. (11). Considering the real-space correlation for the first sharp diffraction peak, $r_F = 5.4$ Å, this radius was taken as the starting point for the range of correlations to be excluded from the sum. It was found that only removing correlations from 7.0 to 7.4 Å gave a good fit to the shift at $k_F = 1.16$ Å^{-1} in the experimental spectrum.[33] At the same time, the computation reproduced the unaltered model $I(k)$ spectrum [Fig. 9(a)] virtually unchanged for $k > 2$ Å^{-1}. In Fig. 9(b) we show side by side the experimental and the simulated spectra for the photodarkened and annealed state for the low-k region. The two sets of curves agree qualitatively in position and relative amplitude, indicating our method points in the right range of correlations. It must be realized, of course, that this simulated shift was obtained by totally unphysical means: the removal of shell contributions to the total scattering intensity. Furthermore, changes in other physical quantities like density are not simulated at all. The result sug-

gests that the modification in the scattering intensity with photodarkening is brought about by changes in correlations in the range from 7.0 to 7.4 Å. Since photodarkening in As$_2$S$_3$ manifests itself by dihedral angle distortions, it can be inferred that the dihedral angle distortions induce changes in the correlations between S atoms on two different AsS$_3$ pyramids joined at a particular S site. This fourth-nearest-neighbor distance occurs at a range of up to 6.5 Å. Thus, our simulated $I(k)$ spectrum for photodarkening points to changes in correlations beyond the fourth-nearest neighbor along a helical chain and also
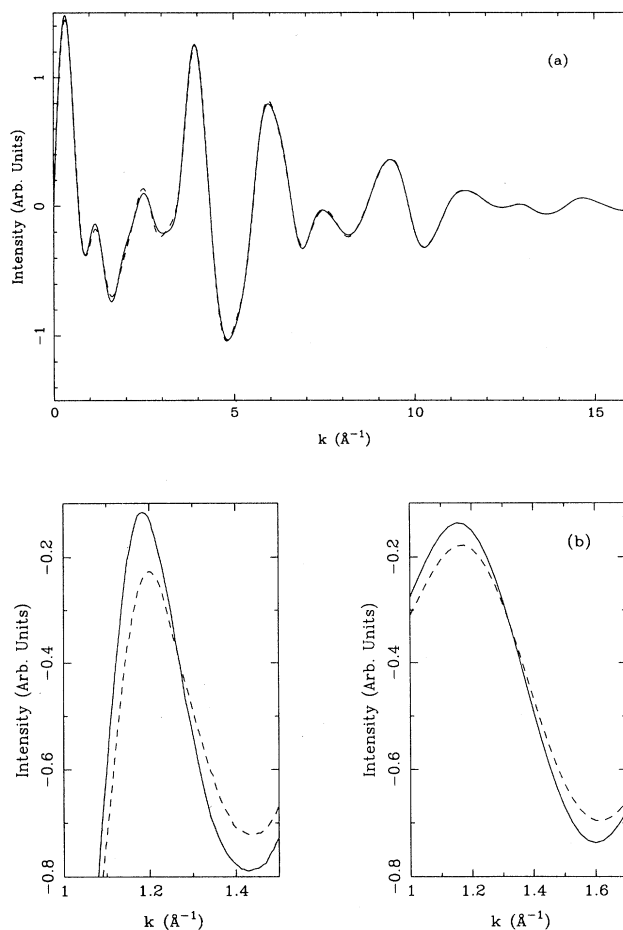

FIG. 9. Changes in reduced x-ray-scattering intensity, $F(k)$, simulated from model A. (a) Comparison of the x-ray-scattering spectrum as calculated from model A by removing all real-space correlations in the range from 7.0 to 7.4 Å (solid line) and the spectrum without the shell removed (dotted line). The annealed state corresponds to the unaltered spectrum, whereas the photodarkened state corresponds to the spectrum with the shell removed. Noticeable differences occur in the region between 1.0 and 2.2 Å^{-1}. (b) Direct comparison between the simulation and experimental data (see Ref. 33) on an expanded scale for the low-k region. The simulated data are given in the left half of the figure and the experimental results are given in the right half of the figure. The photodarkened state is characterized by a lowering in relative amplitude and a shift to higher k for the first sharp diffraction peak. The simulated data match the experimental results on a systematic basis in this region.

possibly to interchain correlations.

Band-structure calculations[19] for a-Se can be taken as another clue for the nature of photodarkening. Intrinsic local defects in Se chains associated with parallel instead of perpendicular alignment of LP orbitals on two neighboring atoms give rise to additional electronic states. Most prominently, states are introduced into the gap at the conduction- and valence-band edges thereby decreasing the optical gap for the material. Hence, dihedral angle distortions offer a possible qualitative explanation for the photodarkening effect in a-Se. Analysis of the EXAFS data for g-As_2S_3 leads us to speculate that the dihedral angle distortions in photodarkened As_2S_3 give rise to modifications in the electronic density of states similar to those calculated for dihedral angle distortions[19] in a-Se.

IV. SUMMARY AND CONCLUSIONS

In this work we have demonstrated that realistic structural models for compound chalcogenide glasses can be built and analyzed to obtain information about elements of IRO. The topological constraints alone that are built into the chemically ordered CRN model introduce a distinctive degree of IRO. Energy relaxation in a potential reflecting covalent-bonding forces and the LP interaction yields density functions and RDF's in good agreement with experimental data for both models. The models exhibit increased ordering in terms of helical structures, thus suggesting that the driving force for helical ordering is the LP interaction. The first sharp diffraction peak in the x-ray-scattering spectrum appears to be sensitive to the IRO. In particular, position and amplitude of the first sharp diffraction peak are reproduced more accurately by model A, which contains more helical elements than model B. Together with the better match for the average density, this evidence indicates that model A is the physically more reasonable one. Hence, helical elements are important structural units in g-As_2S_3 and play a critical role in the real-space correlations responsible for the first sharp peak. The analysis of dihedral angle configurations points out that the model does not include planar structures and, much less, coherence of several planes, supporting the notion that the first sharp diffraction peak can be explained without relying on a layer model for g-As_2S_3. Hence, in the light of all presently available experimental data and a careful choice of the model parameters, we feel that our model is realistic and can be helpful in understanding the structure of g-As_2S_3 by providing information to point further experimental and theoretical research in new directions. Positive identification of the IRO structural units derived from our model as actually existing in the glass remains a difficult task awaiting improved techniques. Future extensions of our work will include the modification of the relaxation algorithm to include a Monte Carlo method to ensure global minimization of the whole structure. Furthermore, a bond-breaking and -reformation mechanism could be incorporated into the algorithm.

Contributions from different correlations to the first sharp diffraction peak were examined for the calculated $I(k)$ spectrum. The removal of correlations in the range from 7.0 to 7.4 Å produces a shift in the first sharp diffraction peak essentially identical to the experimentally observed shift with photodarkening, giving an indication for the range of the mechanism involved. Due to the unphysical method of removing the contributions of certain real-space correlations, the result can be taken only as a hint for the range of correlations affected by photodarkening. By coupling these results with EXAFS data, it is suggested that the shift in the first sharp diffraction peak is related to dihedral angle distortions on atoms of pyramidal units adjacent to the two originally considered units. Hence, these distortions can be inferred as a possible explanation for the photodarkening mechanism. To put the speculation on a firm basis, theoretical band-structure calculations for undistorted and distorted —As—S—As—S—As— helical structures are currently under way.[34] From the experimental side, a new interpretation of x-ray-absorption near-edge structure (XANES) data in terms of the local electronic density of states is being developed and it is anticipated that changes in the electronic density of states might be directly related to photostructural changes.

APPENDIX: MODEL AND RELAXATION PARAMETERS

Model A consists of 166 arsenic and 279 sulfur atoms for a total of 445 atoms. Model B consists of 269 arsenic and 431 sulfur atoms for a total of 700 atoms. The wooden sticks used to represent the bonds were 7.5 cm long in both models. The density for the relaxed structures is 2.99 g/cm^3 for model A and 2.80 g/cm^3 for model B, compared to an experimental value of 3.17 g/cm^3 for g-As_2S_3.

The parameters used in the VFF part of the relaxation potential are $r_0 = 2.27$ Å for the covalent As—S bond length, $\theta^{As-S-As} = 100.9°$ for the As—S—As and $\theta^{S-As-S} = 101.3°$ for the S—As—S bond angles, respectively. The force constants are $k_r = 8.67$ eV/Å^2, $k_\theta^{(As-S-As)} = 2.81$ eV/Å^2, and $k_\theta^{(S-As-S)} = 2.00$ eV/Å^2. For the lone-pair term (4), the parameters are $k_{pt} = k_{cr} = 0.3106$ eV Å and $\psi_0 = \phi_0 = 90°$. The value of $\gamma = 1.006$ Å^{-1} is found by requiring that $\Phi_{lone\ pair}$ decreases by a factor of 100 from a radius of 2.27 Å (one As—S bond length) to 6 Å. The damping factor $\exp(-\alpha r^2)$ for the calculation of the reduced scattering intensity in Eq. (11) uses an empirical value for α of 0.015 Å^{-2} found by adjusting the height of the first peaks in the spectrum to their experimental values.

[1]N. Morimoto, Mineral. J. (Sapporo) **1**, 160 (1960).

[2]J. C. Philipps, C. A. Beevers, and S.E.B. Gould, Phys. Rev. B **21**, 5724 (1980).

[3]G. Lucovsky and R. M. Martin, J. Non-Cryst. Solids **8-10**, 185 (1972).

[4]A. P. DeFonzo and J. Tauc, in *Structure and Excitations of Amorphous Solids,* AIP Conf. Proc. No. 31, edited by G. Lucovsky and F. L. Galeener (AIP, New York, 1976), p. 172; R. J. Kobliska and S. A. Solin, Phys. Rev. B **8**, 1646 (1974).

[5]C. Y. Yang, M. A. Paesler, and D. E. Sayers, Phys. Rev. B **36**, 9160 (1987).

[6]S. R. Elliott, *Physics of Amorphous Materials* (Longman, New York, 1984), pp. 94–103.

[7]Ref. 6, p. 98.

[8]D. E. Polk and D. S. Boudreaux, Phys. Rev. Lett. **31**, 92 (1973).

[9]P. J. Steinhardt, R. Alben, and D. Weaire, J. Non-Cryst. Solids **15**, 199 (1974).

[10]S. R. Elliott and E. A. Davis, Ref. 4, p. 117.

[11]D. Weaire and F. Wooten, in *Solid State Physics,* edited by F. Seitz, H. Ehrenreich, and D. Turnbull (Academic, New York, 1987), Vol. 39, p. 1.

[12]A. L. Renninger, M. D. Rechtin, and B. L. Averbach, J. Non-Cryst. Solids **16**, 1 (1974).

[13]T. Fujiwara, S. Itoh, and M. Okazaki, J. Non-Cryst. Solids **45**, 371 (1981).

[14]T. G. Fowler and S. R. Elliott, J. Non-Cryst. Solids **92**, 31 (1987).

[15]G. Lucovsky, R. J. Nemanich, S. A. Solin, and R. C. Keezer, Solid State Commun. **17**, 1567 (1975).

[16]G. Lucovsky (private communication).

[17]M. Kastner, Phys. Rev. B **7**, 5237 (1973).

[18]J. Robertson, Philos. Mag. **34**, 13 (1976).

[19]C. K. Wong, G. Lucovsky, and J. Bernholc, J. Non-Cryst. Solids **97&98**, 1171 (1987).

[20]E. Mooser, I. Ch. Schlüter, and M. Schlüter, J. Phys. Chem. Solids **35**, 1269 (1974).

[21]D. Gerlich, E. Litov, and O. L. Anderson, Phys. Rev. B **20**, 2529 (1979).

[22]M. G. Duffy, D. S. Bordeaux, and D. E. Polk, J. Non-Cryst. Solids **15**, 435 (1974).

[23]M. F. Daniel, A. J. Leadbetter, A. C. Wright, and A. N. Sinclair, J. Non-Cryst. Solids **32**, 271 (1979).

[24]M. A. Paesler, J. M. Lee, and G. Pfeiffer, Philos. Mag. Lett. **56**, 203 (1987).

[25]Ref. 6, pp. 61–71.

[26]A. J. Leadbetter and A. J. Apling, J. Non-Cryst. Solids **15**, 250 (1974).

[27]J. C. Phillips, J. Non-Cryst. Solids **34**, 153 (1979).

[28]L. Cervinka, in *The Structure of Non-Crystalline Materials 1982,* edited by P. H. Gaskell, J. M. Parker, and E. A. Davis (Taylor and Francis, London, 1983), p. 255.

[29]L. E. Busse, Phys. Rev. B **29**, 3639 (1984).

[30]A. C. Wright, R. N. Sinclair, and A. J. Leadbetter, J. Non-Cryst. Solids **71**, 295 (1985).

[31]K. Tanaka, in *Fundamental Physics of Amorphous Semiconductors,* edited by F. Yonezawa (Springer-Verlag, New York, 1981), p. 104, and references therein.

[32]Ke. Tanaka, J. Non-Cryst. Solids **59&60**, 925 (1983).

[33]K. Tanaka, Appl. Phys. Lett. **26**, 243 (1975).

[34]D. Babic, J. Bernholc, and S. Rabii, Phys. Rev. B (to be published).